The Astrophysical Journal, 931:7 (16pp), 2022 May 20 https://doi.org/10.3847/1538-4357/ac6104

Multiwavelength Variability of Sagittarius A* in 2019 July

H. Boyce[1,2], D. Haggard[1,2], G. Witzel[3], S. von Fellenberg[3], S. P. Willner[4], E. E. Becklin[5], T. Do[6], A. Eckart[3,7], G. G. Fazio[4], M. A. Gurwell[4], J. L. Hora[4], S. Markoff[8,9], M. R. Morris[5], J. Neilsen[10], M. Nowak[11], H. A. Smith[4], and S. Zhang[12]
[1] Department of Physics, McGill University, 3600 University Street, Montréal, QC H3A 2T8, Canada; hope.boyce@mail.mcgill.ca
[2] McGill Space Institute, McGill University, 3550 University Street, Montréal, QC H3A 2A7, Canada
[3] Max-Planck-Institut für Radioastronomie, Auf dem Hügel 69, D-53121, Bonn, Germany
[4] Center for Astrophysics | Harvard & Smithsonian, 60 Garden Street, Cambridge, MA 02138-1516, USA
[5] Department of Physics and Astronomy, University of California, Los Angeles, CA 90095-1547, USA
[6] UCLA Galactic Center Group, Physics and Astronomy Department, University of California, Los Angeles, CA 90024, USA
[7] Institute of Physics, University of Cologne, Zülpicher Straße 77, D-50937 Cologne, Germany
[8] Anton Pannekoek Institute for Astronomy, University of Amsterdam, Science Park 904, 1098 XH Amsterdam, The Netherlands
[9] Gravitation Astroparticle Physics Amsterdam (GRAPPA) Institute, University of Amsterdam, Science Park 904, 1098 XH Amsterdam, The Netherlands
[10] Villanova University, Mendel Science Center Room 263B, 800 East Lancaster Avenue, Villanova, PA 19085, USA
[11] Physics Department, Washington University, CB 1105, St. Louis, MO 63130, USA
[12] Bard College, 30 Campus Road, Annandale-on-Hudson, NY 12504, USA
Received 2021 December 3; revised 2022 March 3; accepted 2022 March 23; published 2022 May 18

Abstract

We report a timing analysis of near-infrared (NIR), X-ray, and submillimeter data during a 3 day coordinated campaign observing Sagittarius A*. Data were collected at 4.5 μm with the Spitzer Space Telescope, 2–8 keV with the Chandra X-ray Observatory, 3–70 keV with NuSTAR, 340 GHz with ALMA, and 2.2 μm with the GRAVITY instrument on the Very Large Telescope Interferometer. Two dates show moderate variability with no significant lags between the submillimeter and the infrared at 99% confidence. A moderately bright NIR flare ($F_{\rm K} \sim 15$ mJy) was captured on July 18 simultaneous with an X-ray flare ($F_{2-10\ \rm keV} \sim 0.1$ counts s^{-1}) that most likely preceded bright submillimeter flux ($F_{340\ \rm GHz} \sim 5.5$ Jy) by about $+34^{+14}_{-33}$ minutes at 99% confidence. The uncertainty in this lag is dominated by the fact that we did not observe the peak of the submillimeter emission. A synchrotron source cooled through adiabatic expansion can describe a rise in the submillimeter once the synchrotron self-Compton NIR and X-ray peaks have faded. This model predicts high GHz and THz fluxes at the time of the NIR/X-ray peak and electron densities well above those implied from average accretion rates for Sgr A*. However, the higher electron density postulated in this scenario would be in agreement with the idea that 2019 was an extraordinary epoch with a heightened accretion rate. Since the NIR and X-ray peaks can also be fit by a nonthermal synchrotron source with lower electron densities, we cannot rule out an unrelated chance coincidence of this bright submillimeter flare with the NIR/X-ray emission.

Unified Astronomy Thesaurus concepts: Galactic center (565); Black hole physics (159); Accretion (14); Non-thermal radiation sources (1119); Supermassive black holes (1663)

1. Introduction

Sagittarius A* (Sgr A*), the supermassive black hole (SMBH) sitting at the bottom of the central gravitational potential of the Milky Way, coexists in a dynamic environment with a dense stellar cluster, active star formation, and hot, inefficiently accreting gas. Over the past ∼20 yr, the mass ($\sim 4 \times 10^6\ M_\odot$) and accretion rate ($\lesssim 10^{-7}\ M_\odot\ \rm yr^{-1}$) of Sgr A* have been pinned down through careful analysis of stellar orbits (e.g., Boehle et al. 2016; Gillessen et al. 2017) and multiwavelength flux measurements (e.g., Baganoff et al. 2003; Marrone et al. 2006, 2007; Shcherbakov et al. 2012; Yusef-Zadeh et al. 2015; Bower et al. 2018). These properties, along with its low bolometric-to-Eddington luminosity ratio ($L/L_{\rm Edd} \sim 10^{-9}$; Genzel et al. 2010) and characterizations of the quiescent spectral energy distribution (SED), have motivated models of advective and inefficient accretion flows (e.g., Quataert 2002; Baganoff et al. 2003; Yuan et al. 2003; Liu et al. 2004; Xu et al. 2006; Wang et al. 2013).

Though Sgr A* seems to be variable at every wavelength at which it has been observed, the physical mechanisms behind the changes in Sgr A*'s flux density remain uncertain. Physical models often invoke populations of accelerated electrons caused by magnetic reconnection events, jets, sudden disk instabilities, or other stochastic processes in the accretion flow (e.g., Markoff et al. 2001; Liu & Melia 2002; Yuan et al. 2003; Liu et al. 2004; Dexter et al. 2009; Maitra et al. 2009; Dodds-Eden et al. 2010; Ball et al. 2016; Li et al. 2017). Additional models attempt to explain the variability in the context of tidal disruption of asteroids (Čadež et al. 2008; Kostić et al. 2009; Zubovas et al. 2012) or expanding plasma blobs (e.g., van der Laan 1966; Yusef-Zadeh et al. 2006a; Marrone et al. 2008; Younsi & Wu 2015; Li et al. 2017). Finally, emission may be amplified through strong gravitational lensing near the event horizon (e.g., Chan et al. 2015).

Variability in the near-infrared (NIR) is expected to arise from a fluctuating nonthermal population of electrons. Chen et al. (2019) showed that Sgr A*'s IR variability was statistically consistent over two decades, never deviating from

a lognormal distribution of flux densities. This consistency was immediately challenged by the unprecedented IR brightness detected by Do et al. (2019) in 2019 March. Such a deviation from the usual statistical behavior (Do et al. 2009; Meyer et al. 2009; Dodds-Eden et al. 2011; Witzel et al. 2012; Hora et al. 2014; Witzel et al. 2018) challenges the current model and could point to a dynamical interaction or temporary change in Sgr A*'s accretion state.

The submillimeter–THz bump in Sgr A*'s SED is often attributed to a steady synchrotron source originating from a thermal electron distribution (e.g., Bower et al. 2018; von Fellenberg et al. 2018). Submillimeter flux from Sgr A* is variable down to timescales of seconds to hours (Iwata et al. 2020; Murchikova & Witzel 2021), suggesting source sizes on the same order as the BH's innermost stable orbit. Dexter et al. (2014) found an 8 hr characteristic timescale for the variability by analyzing light curves over a period of 10 yr. Subroweit et al. (2017) presented a statistical analysis of submillimeter variability at 345 GHz from 2008 to 2014, reporting a mean flux density measurement of ∼3 Jy. In 190 hr of observations, the 345 GHz flux rose above 4.5 Jy only four times. Murchikova & Witzel (2021) reported observations of Sgr A* at 230 GHz in 2019 June, finding that the mean flux level was 3.74 Jy, 20% higher than in 2015–2017 and 3% higher than in 2009–2012 and 2013–2014. Such variability (on the scale of ∼10 yr) is similar to the expected global mass accretion variability (Ressler et al. 2020).

Sgr A*'s faint, steady X-ray emission (Baganoff et al. 2001, 2003) is most likely thermal bremsstrahlung emission originating in the accretion flow near the Bondi radius (Quataert 2002; Baganoff et al. 2003; Yuan et al. 2003; Liu et al. 2004; Xu et al. 2006; Wang et al. 2013). This quiescent state is interrupted about once per day by distinct X-ray flares of nonthermal emission presumed to be coming from very close to the BH (Neilsen et al. 2013, 2015; Haggard et al. 2019; Zhang et al. 2017). The flux density distribution of the X-ray variability can be described by a power law (e.g., Neilsen et al. 2015) or lognormal (Witzel et al. 2021). Recent examination of long-term X-ray variability suggests that Sgr A*'s flaring rate can change over the span of several years (Andrés et al. 2022).

There have been several studies reporting a correlation between submillimeter and NIR/X-ray variability (e.g., Eckart et al. 2006b; Yusef-Zadeh et al. 2006b; Eckart et al. 2008b; Yusef-Zadeh et al. 2009; Trap et al. 2011; Eckart et al. 2012; Mossoux et al. 2016; Fazio et al. 2018). These provide increasing evidence that the submillimeter and NIR/X-ray sources are physically or radiatively connected. Correlations between the radio and NIR remain less clear (Capellupo et al. 2017).

To connect physical models with observables, studies have analyzed the timing properties between wavelengths and SED characteristics of Sgr A* during quiescence and flares. They aim to put constraints on what radiative mechanisms must be at play. For example, there are models that predict simultaneity of NIR/X-ray flares through synchrotron self-Compton (SSC) processes (Markoff et al. 2001; Eckart et al. 2008a), those that cool the electrons of the synchrotron source to predict delayed low-frequency emission relative to the NIR/X-ray (e.g., Yusef-Zadeh et al. 2006b; Witzel et al. 2021), and those that connect time lags to relativistic outflows (e.g., Brinkerink et al. 2021). General relativistic magnetohydrodynamic (GRMHD) simulations also predict radiative models and observable SED characteristics scaled to Sgr A* (e.g., Mościbrodzka et al. 2009, 2014) and even simulate light curves comparable to observations (Chatterjee et al. 2021).

There are several observational avenues that can be used to constrain the properties of the plasma in the galactic center. Observations of a magnetar at an angular distance of ∼2.″5 from Sgr A* (Mori et al. 2013; Rea et al. 2013) have been useful in constraining the interstellar scattering that affects observations in the vicinity of the SMBH (e.g., Bower et al. 2015; Dexter et al. 2017). Such observations can constrain the properties of the plasma and magnetic field (e.g., Eatough et al. 2013). Even closer to the BH, new observations by the Event Horizon Telescope (EHT; e.g., Issaoun et al. 2021) and GRAVITY are beginning to probe the plasma and general relativistic effects near the event horizon. Observations of Sgr A* with EHT were collected in 2017, 2018, 2021, and 2022. Such high-resolution imaging will help untangle the dynamics of the plasma immediately around Sgr A* from the significant interstellar scattering between Earth and the Galactic center (e.g., Johnson et al. 2018; Issaoun et al. 2019). Also probing near event horizon scales, the GRAVITY Collaboration has demonstrated that exceptionally precise NIR interferometry of Sgr A*'s position can probe the apparent motion of its centroid. This, in turn, can be successfully modeled as a hot spot orbiting less than 10 gravitational radii away from the SMBH (Gravity Collaboration et al. 2018).

Numerous joint X-ray and IR campaigns have observed Sgr A* over the last 16 yr (Eckart et al. 2004, 2006b; Yusef-Zadeh et al. 2006b; Eckart et al. 2008a; Dodds-Eden et al. 2009; Yusef-Zadeh et al. 2009, 2012; Mossoux et al. 2016; Ponti et al. 2017; Fazio et al. 2018). Our joint Spitzer and Chandra study reported ∼144 hr of coordinated observations collected between 2014 and 2017 (Boyce et al. 2019). These observations captured four modestly bright multiwavelength flares from Sgr A*. Comparing the X-ray observations to simulations of the infrared statistical behavior (Witzel et al. 2018), the consistent observation of X-ray and IR events within 20 minutes of each other point to a physical connection between the emission at these wavelengths, rather than chance association. In Boyce et al. (2019), we found that the time lag between the peaks in the X-rays and the peaks in the IR was consistent with simultaneity and at most on order of 10–20 minutes with 68% significance.

Here we extend our original study by investigating the physical and temporal correlations between X-ray and IR variability with Spitzer and Chandra observations of Sgr A* in the summer of 2019, alongside simultaneous NuSTAR, GRAVITY, and Atacama Large Millimeter/submillimeter Array (ALMA) monitoring. To constrain the particle accretion responsible for flaring, Abuter et al. (2021) analyzed the Spitzer, GRAVITY, NuSTAR, and Chandra data of July 17 −18 in the context of time-resolved SED modeling and found that the NIR and X-ray flare can be best modeled with a nonthermal synchrotron source. Michail et al. (2021) combined the Spitzer NIR measurements with the 340 GHz ALMA measurements on July 18 to explore models that describe the NIR as SSC of a synchrotron source responsible for delayed submillimeter emission adiabatically expanding. Bringing all available data together, this paper reports timing analyses between the five observatories on July 17−18, July 21, and July 26 and explores how SED models (see Section 4) can be constrained by the submillimeter, NIR, and X-ray timing data.

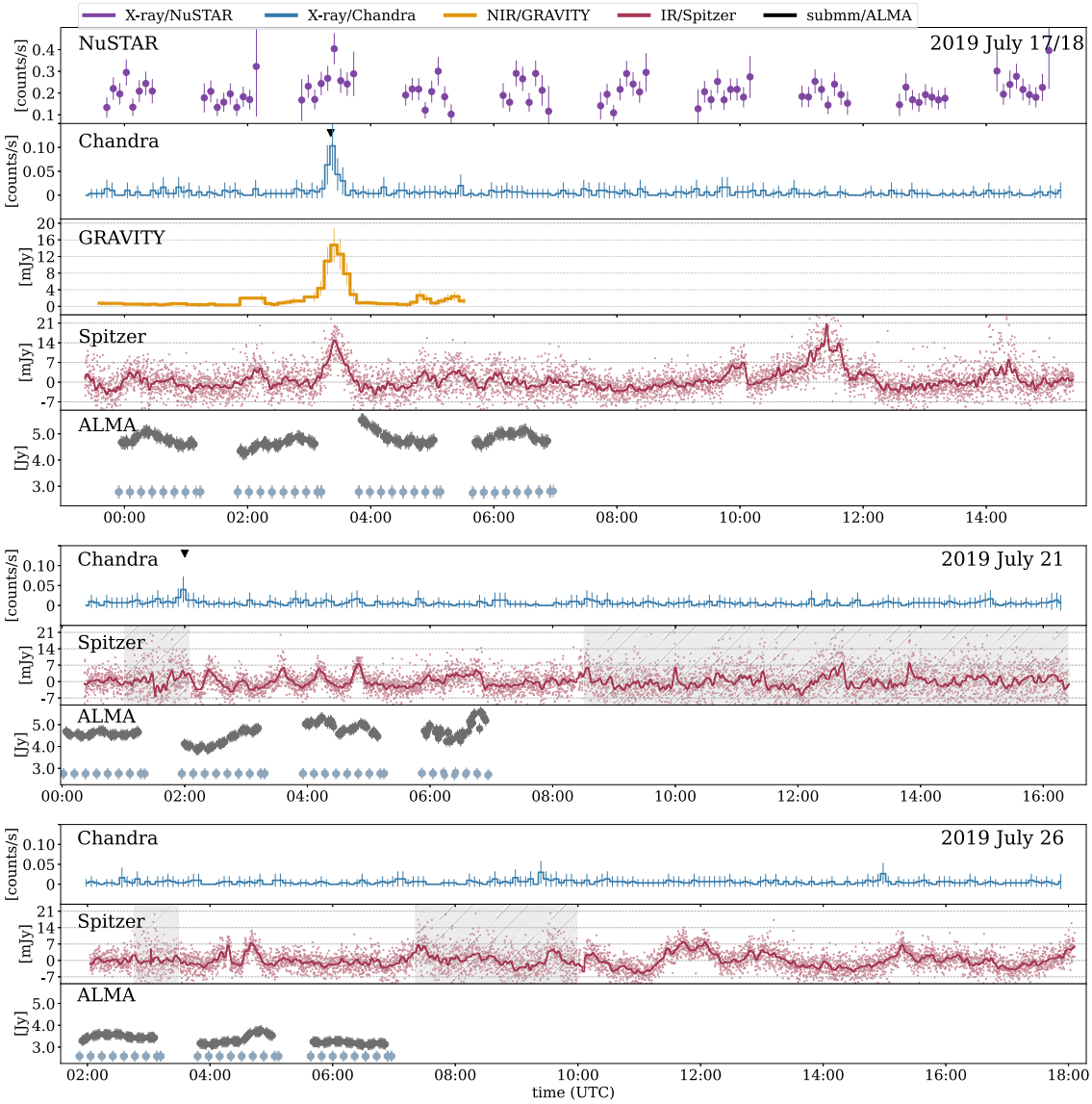

Figure 1. Simultaneous submillimeter, IR, and X-ray light curves of Sgr A* from 2019 July. The purple, blue, orange, red, and gray data show the NuSTAR 3–70 keV, Chandra 2–8 keV, GRAVITY 2.2 μm, Spitzer 4.5 μm, and ALMA 340 GHz data, respectively. The *x*-axis displays the barycenter-corrected UT on each date. Spitzer data at 4.5 μm are the excess flux density (mJy) of the pixel containing Sgr A* (see Section 2.1 of Witzel et al. 2018) offset with a value of 1.9 mJy and dereddened with the extinction $A_{\rm Ks} = 2.42 \pm 0.002$ from Fritz et al. (2011). The red line shows the data binned over 3.5 minutes. Gray regions on July 21 and 26 indicate where the light curve is unreliable due to a decreased signal-to-noise ratio. The GRAVITY light curve was dereddened assuming a *K*-band extinction of 2.42 ± 0.01 mag. Significant X-ray flares in the Chandra data are identified by the Bayesian blocks routine ($p_0 = 0.05$) and indicated here with black triangles. ALMA calibrators are plotted in light gray for comparison.

2. Observations and Data Reduction

The IRAC instrument (Fazio et al. 2004) on the Spitzer Space Telescope (Werner et al. 2004) observed Sgr A* at 4.5 μm for eight ~24 hr long stretches between 2013 and 2017. Six of these observations had simultaneous monitoring from the Chandra X-ray Observatory (Weisskopf et al. 2000) and are reported by Boyce et al. (2019). Since then, three additional epochs of simultaneous monitoring totaling ~48 hr were observed. These additional epochs expand the total data set to ~155 hr of simultaneous X-ray and IR data. Figure 1 displays these new 2019 epochs along with additional coordinated coverage from NuSTAR, GRAVITY, and ALMA. Table 1 lists the details of these datasets. For an assumed distance of 8.2 kpc, $1'' = 0.040$ pc (Gravity Collaboration et al. 2019).[13]

[13] 7.9 kpc would give $1'' = 0.038$ pc (Boehle et al. 2016).

2.1. Spitzer

All Spitzer observations were collected in a similar manner as the previous epochs in the campaign. Hora et al. (2014) gave a complete description of the Sgr A* Spitzer monitoring campaign. We offer a brief summary here. Three observing blocks were collected at 4.5 μm (filter width of 1 μm) in each of the three 16 hr epochs: an initial mapping operation performed after the slew to the Sgr A* field followed by two successive 8 hr staring operations. Each staring operation began by using the "PCRS Peakup" mode to position Sgr A* on the center of the pixel (16, 16) in the IRAC subarray. The subarray mode for Spitzer/IRAC reads out 64 consecutive images (a "frame set") of a 32×32 pixel region on the IRAC detector. This frame set is known as one basic calibrated data (BCD) product, which is the data format downloaded from the

Table 1
Data Sets Analyzed in This Work

Observatory	Date (UT)	ObsID	Start (UT)	End (UT)	Energy	Wavelength (frequency)	No. of Ant.	Baselines (kλ)	Calibrators
NuSTAR	2019-07-17	30502006002	21:51:09	08:34:21	3−70 keV	6.2−0.2 Å	⋯	⋯	⋯
	2019-07-26	30502006004	00:41:09	10:21:06	3−70 keV	6.2−0.2 Å	⋯	⋯	⋯
Chandra	2019-07-17	22230	22:51:26	14:51:26	2−8 keV	6.2−1.6 Å	⋯	⋯	⋯
	2019-07-21	20446	00:00:14	16:00:14	2−8 keV	6.2−1.6 Å	⋯	⋯	⋯
	2019-07-26	20447	01:32:40	17:32:40	2−8 keV	6.2−1.6 Å	⋯	⋯	⋯
GRAVITY	2019-07-17	0103.B-0032(D)	23:32:55	05:32:55	0.7−0.8 eV	2.2−1.65 μm	⋯	⋯	⋯
Spitzer	2019-07-17	69965312	23:21:33	07:21:20	0.3 eV	4.5 μm	⋯	⋯	⋯
	2019-07-18	69965568	07:25:02	15:24:49	0.3 eV	4.5 μm	⋯	⋯	⋯
	2019-07-21	69965824	00:21:47	08:21:37	0.3 eV	4.5 μm	⋯	⋯	⋯
	2019-07-21	69966080	08:24:49	16:25:05	0.3 eV	4.5 μm	⋯	⋯	⋯
	2019-07-26	69966336	02:02:35	10:02:22	0.3 eV	4.5 μm	⋯	⋯	⋯
	2019-07-26	69966592	10:06:02	18:05:53	0.3 eV	4.5 μm	⋯	⋯	⋯
ALMA	2019-07-17	2018.A.00050.T	23:49:02	06:49:56	0.0014 eV	[340 GHz]	11	10.1−54.4	J1700–2610 J1733–3722
	2019-07-20	2018.A.00050.T	03:55:59	06:47:57	0.0014 eV	[340 GHz]	11	10.1−54.4	J1700–2610
	2019-07-25	2018.A.00050.T	23:51:49	06:45:15	0.0014 eV	[340 GHz]	10	10.1−54.4	J1717–3342

Spitzer Heritage Archive.[14] Each component in the frame set is a 0.1 s 32 × 32 image, so one frame set takes 6.4 s to complete. After converting the pixel intensity into mJy, each frame set was combined into a single 32 × 32 image referred to as a "6.4 s BCD coadd." Consecutive frame sets were typically separated by 2 s of telescope overheads, and this resulted in an observation cadence of approximately 8.4 s per frame.

To extract light curves of Sgr A* from the Spitzer/IRAC data, we used the same methodology as Boyce et al. (2019) and Witzel et al. (2018), including an updated procedure based on the steps described in Appendix A1 of Hora et al. (2014). This procedure corrects for the varying intrapixel sensitivity of the Spitzer/IRAC detector and the effect of nearby sources on the measured flux of Sgr A* as the telescope pointing jitters during the observations. The resulting light curves are the excess variable flux density in pixel (16, 16) measured relative to the nonvariable stellar background (∼250 mJy). The baseline flux density of these IR light curves is unknown, though the value has been inferred to be 1.9 mJy from the cumulative distributions of flux densities of Sgr A* (Witzel et al. 2018). As in Abuter et al. (2021), we added an offset of 1.9 mJy and dereddened the resulting values with the extinction $A_{\rm Ks} = 2.42 \pm 0.002$ from Fritz et al. (2011) to produce the light curves plotted in Figure 1.

2.2. Chandra

The simultaneous Chandra observations were acquired using the ACIS-S3 chip in the FAINT mode with a 1/8 subarray. The small subarray was chosen to avoid photon pileup during bright flares from Sgr A* and the nearby magnetar, SGR J1745−2900 (Mori et al. 2013; Rea et al. 2013; Coti Zelati et al. 2015, 2017).

We performed Chandra data reduction and analysis with CIAO v4.9 tools[15] (Fruscione et al. 2006) and calibration database 4.7.3. The `chandra_repro` script was used to reprocess level 2 events files before the WCS coordinate system was updated (`wcs_update`). Barycentric corrections to the event times were performed with the CIAO tool `axbary`. We extracted a 2–8 keV light curve from a circular region of radius 1.″25 centered on Sgr A*. The small extraction region and energy range isolate Sgr A*'s emission from the nearby magnetar (e.g., Mori et al. 2013; Rea et al. 2013; Coti Zelati et al. 2017) and the diffuse X-ray background (e.g., Baganoff et al. 2003; Nowak et al. 2012; Wang et al. 2013). The X-ray light curves are plotted in purple in Figure 1. Flux densities for SED modeling (Section 4) were corrected for dust scattering and absorption as described in Abuter et al. (2021).

2.3. NuSTAR

The NuSTAR (Harrison et al. 2013) data have been processed using the NuSTAR Data Analysis Software NUSTARDAS, HEASOFT v. 6.28, and CALDB v20200912. Data were filtered for periods of high instrumental background due to South Atlantic Anomaly passages and known bad detector pixels. We analyzed the observations starting on 2019 July 17 21:51:09 and 2019 July 26 00:41:09 (ObsIDs: 30502006002 and 30502006004, respectively). We applied the barycenter corrections. Light curves and spectra were extracted via the `nuproducts` tool from a region of radius 20″ centered on the position of Sgr A*. Because the focal plane module B (FPMB) is contaminated by stray light from faraway bright X-ray sources outside of the field of view, we only present the analysis of the FPMA data (the results obtained with FPMB are consistent with the results). The light curves were accumulated in the 3−10 keV band and with 380 s time bins for comparison with the GRAVITY data. Bins with small fractional exposures were removed. Flux densities for SED modeling (Section 4) were corrected for dust scattering and absorption as described in Abuter et al. (2021).

2.4. GRAVITY

The *K*-band (2.1−2.4 μm) GRAVITY light curve was derived from the coherent flux measurement of Sgr A* as described by

[14] The Spitzer Heritage Archive (http://irsa.ipac.caltech.edu) is part of the NASA/IPAC Infrared Science Archive, which is operated by the Jet Propulsion Laboratory, California Institute of Technology, under contract with the National Aeronautics and Space Administration.
[15] Chandra Interactive Analysis of Observations (CIAO) software is available at http://cxc.harvard.edu/ciao/.

Gravity Collaboration et al. (2020b) and Abuter et al. (2021). We derived the flux ratios relative to S2 using separate observations. We dereddened the flux assuming a *K*-band extinction of 2.42 ± 0.01 mag. The light curve has been corrected for the contamination of S2 at the edge of the field of view, and the errors were scaled in the same way as described in Gravity Collaboration et al. (2020b). We ignored the contribution of the faint star S62 (Gravity Collaboration et al. 2021), which should amount to less than 0.1 mJy. The *H*-band light curve was also reduced but not used here, as the lower signal-to-noise ratio provided negligible improvement over the *K*-band data in constraining the timing. See Abuter et al. (2021) for details.

2.5. ALMA

All three epochs of Spitzer data presented here were partly covered by ALMA observations.[16] Sgr A* was observed using the 7 m ALMA compact array on July 17/18 (see also Michail et al. 2021), 21, and 26 in 2019. With 11 and 10 (epoch of July 25/26) antennas, this compact configuration has 55 and 45 unique projected baselines, respectively, from 8.904 to 47.987 m (10.1 to 54.4 kλ). The corresponding maximal resolution is 4.″6. The total continuum bandwidth was 2 GHz.

The quality assessment of the epochs by the ALMA pipeline was "semipass" for the first two epochs and "pass" for the last epoch.[17] Each epoch consisted of four observation blocks on Sgr A*, each ∼76 minutes, with seven scans of ∼7 minutes duration and an eighth scan that is shorter than 1 minute. Between each scan, there is a gap of ∼4 minutes, and between the observation blocks, there are gaps of ∼40 minutes. The data quality particularly suffered from the atmospheric conditions in the last observing block of each of the first two epochs, while all other blocks are of comparable quality.

Bandpass and gain were calibrated using calibrators J1337−1257 (block 1 of each epoch) and J1924−2914 (blocks 2−4 of each epoch). Gain and phase calibration were executed using calibrators J1700−2610 (epoch 1, blocks 1−3; epoch 2), J1733−3722 (epoch 1, block 4), and J1717−3342 (epoch 3) in alternation with measurements of Sgr A*.

To derive light curves, we first restored the gain-calibrated visibilities with the scripts `scriptForPi.py`, which are part of the data archive. The resulting visibilities were then separated by source and spectral range. For each spectral window with science data (16, 18, 20, and 22), we chose the frequency range dominated by continuum emission as identified by the routine `hif_findcont` of the ALMA pipeline. We then applied three iterations of fitting a point-source model to the visibilities (with the CASA routine `uvmodelfit`) and interleaved phase self-calibration (with the CASA routines `gaincal` and `applycal`). After a fourth fit with a point-source model, we used the resulting flux density as our measurement. This algorithm was applied to visibilities of Sgr A* and the particular phase calibrator in time windows of 1 minute. The last 1 minute bin of each scan with just a few data points, as well as the last scans of observations blocks that are shorter than 1 minute, were discarded.

The resulting light curves have a regular cadence of 1 minute and a total duration of 7 hr with 5 hr of data each. Heliocentric corrections of +7.366, +7.158, and +6.772 minutes were applied for the comparison with the Spitzer light curves. We estimate the absolute flux density calibration to be accurate within 10% uncertainty and the relative photometric precision to be <3%.

[16] Project 2018.A.00050.T; PI: J.Carpenter.

[17] Criteria described in the ALMA technical handbook, https://almascience.nrao.edu/documents-and-tools/cycle7/alma-technical-handbook/view.

3. Analysis

3.1. Flare Characterization

To identify significant X-ray flares, we used the Bayesian blocks algorithm as described by Scargle (1998) and Scargle et al. (2013) and provided as a python routine by Peter K. G. Williams (`bblocks`; Williams et al. 2017). We ran the algorithm using a 95% confidence interval (a false-positive rate of $p_0 = 0.05$). This choice for p_0 implies that the probability that a change point is real is $1 - 0.05 = 95\%$, and the probability that a flare (at least two change points) is real is $1 - (p_0)^2 = 99.8\%$. Detected flares are indicated by triangles in Figure 1.

We detected two Chandra X-ray flares during the total overlap period of X-ray and IR, one on 2019 July 18 and one on 2019 July 21. The detection rate is consistent with past measurements of the average number of X-ray flares from Sgr A* (∼1.1 day^{-1}; Neilsen et al. 2015; Ponti et al. 2015). The mean quiescent flux measured with Chandra during these epochs was 0.005 counts s^{-1}, and while the flare detected on 2019 July 21 was similar to those reported by Boyce et al. (2019; 20 counts), the flare detected on 2019 July 18 had a total of 74 counts and was not bright enough for pileup to significantly affect the measurement.

In contrast to the distinct peaks in the X-rays, the emission from Sgr A* at IR wavelengths is constantly varying. An apparent quasiperiodic feature appears in the Spitzer light curve on July 21. Such apparent periodicities can appear in processes described by correlated red noise, and the statistics of Sgr A*'s NIR variability is well described by a red-noise process (e.g., Do et al. 2009; Witzel et al. 2012). There are also multiple IR peaks where we see no significant X-ray emission, even in cases when the IR emission is most elevated (e.g., ∼6 mJy around 11:30 July 18), whereas the X-ray flare on July 18 was accompanied by a significant rise in the NIR flux density levels. This behavior (NIR peaks accompanying X-ray flares but not the reverse) is consistent with all previous reported X-ray/IR observations of Sgr A*, as well as recent simulations (e.g., Witzel et al. 2021). We do not consider the X-ray flare with a lack of NIR rise around 02:00 July 21 as contradictory because the IRAC data exhibited higher-than-normal noise levels at this time due to poor stability in the telescope pointing. A rise in the submillimeter flux at 06:30 on July 21 was not accompanied by corresponding variability X-ray and has marginally significant higher-than-average variability in the NIR. Additionally, on July 26, IR variability was observed along with a rise in the submillimeter but with no corresponding flare in the X-ray.

With a *K*-band peak flux density of ∼16 mJy, the NIR flare on July 18 can be classified as moderately bright in the context of previously observed variability (Abuter et al. 2021), while the X-ray flare was fairly modest with a peak of 0.1 counts s^{-1}. This is a factor of ∼2 brighter than the four faint flares with simultaneous Spitzer data reported by Boyce et al. (2019) but a factor of ∼14 lower than the brightest X-ray flare observed (Haggard et al. 2019). The brightest flare observed simultaneously in NIR and X-rays was reported by Dodds-Eden et al. (2009) and had an *L*-band flux density of ∼25 mJy and the 2–10 keV X-ray flare reaching ∼1 counts s^{-1}. While the X-ray

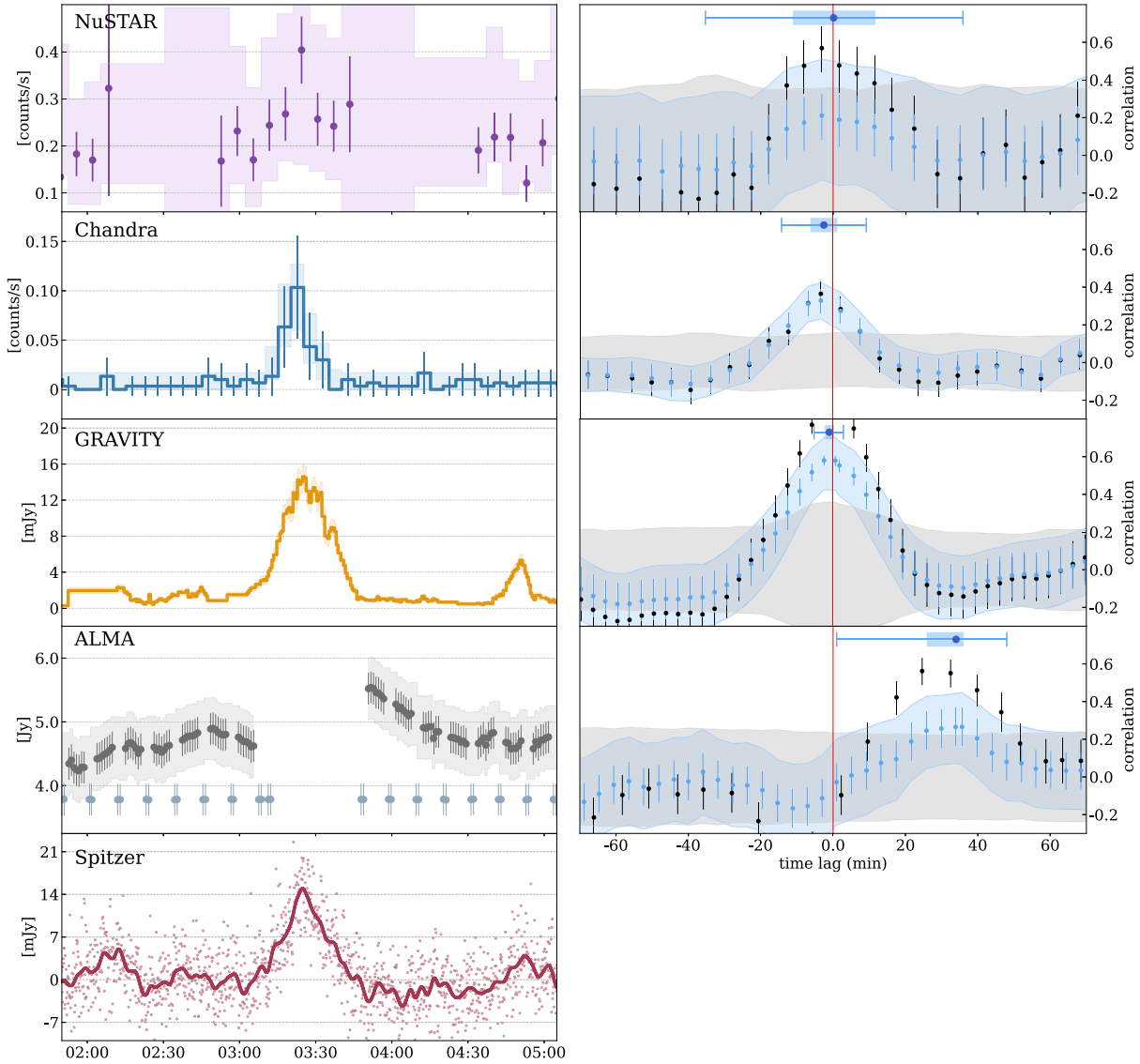

Figure 2. Results from running ZDCF on the NuSTAR (purple), Chandra (blue), GRAVITY (orange), and ALMA (gray) light curves against the respective Spitzer (red) light curve on 2019 July 17/18. Left panels: regions of the multiwavelength light curves during the X-ray/NIR flare. Their respective envelopes show the 95% range of the 10,000 MC realizations. The x-axis displays the UTC time since the start of the Spitzer/IRAC observations. The bottom panels show the ZDCF. In the right panels, the blue points are the average cross-correlation of all 10,000 MC realizations, with the blue envelope capturing the 95% range. The gray envelope is the 95% range from the IR MC realizations with 10,000 realizations of simulated noise consistent with the characteristics of the second light curve's emission (no flares). The significant time lags and confidence intervals are plotted as a single blue point in each panel, with the 68% interval represented by the blue shaded box and the 99.7% interval represented by the thin error bar.

and NIR variability was moderate on July 18, this does not hold for 340 GHz, which, at the highest point, was 5.5 Jy, well above the typically measured quiescent levels of ∼3 Jy (Subroweit et al. 2017). In fact, the mean flux density (∼4.5 Jy) measured on July 18 and July 21 was also elevated with respect to historic levels.

3.2. Multiwavelength Timing

During the Chandra X-ray flare on July 18, the emission from Sgr A* at 4.5 and 2.2 μm rose within minutes of the X-ray peak. Nearly simultaneously, NuSTAR detected moderate X-ray variability through a measurement of increased count rate in a single 6 minute bin. At 340 GHz, ALMA observations also captured part of this flare but missed the peak (Figure 2).

To quantify the lags between the peaks of potentially associated activity in the these observations, we followed Boyce et al. (2019). We utilized the FORTRAN 95 implementation[18] of the z-transform discrete correlation function (ZDCF; Alexander 1997). This tool estimates the cross-correlation function of two inputs without a penalty for having a sparse or unevenly sampled light curve. We cross-correlated all observations relative to the simultaneous 4.5 μm Spitzer light curves binned at 3.5 minutes (red in Figures 1 and 2), which cover nearly all of the observing time of the other observatories.

To estimate the uncertainties in the measured time lags, we cross-correlated each pair of data over 10,000 Monte Carlo (MC) iterations. Bins of 3.5 minutes were chosen for the Spitzer data to increase the efficiency of the cross-correlation MC. Experiments with smaller bins yielded time lags consistent with the results presented here. The uncertainty on the time lags

[18] Found at www.weizmann.ac.il/weizsites/tal/research/software/.

Table 2
Time Delays with Respect to 4.5 μm (Spitzer) for X-Ray (NuSTAR, Chandra), $\sim$2 μm (GRAVITY), and 340 GHz (ALMA) Variability

Instrument	Time Lag (minutes)	68% Interval	99.7% Interval
2019 July 18			
NuSTAR	$+2^{+15}_{-15}$	(−13, +16)	(−47, 48)
Chandra	-3^{+3}_{-3}	(−6, +0)	(−12, +7)
GRAVITY	$+0^{+1}_{-3}$	(−3, +1)	(−9, +9)
ALMA	$+34^{+2}_{-8}$	(+26, +36)	(+1, +48)
2019 July 21			
ALMA	$+27^{+12}_{-60}$	(−33, +39)	(−48, +46)
2019 July 26			
ALMA	$+20^{+14}_{-14}$	(+6, +35)	(−39, +44)

Note. Positive values mean that the peaks lag Spitzer peaks. Uncertainties on the time lag in the second column span the 68% confidence interval on the 10,000 MC runs. The third column displays the boundaries of this 68% confidence interval, while the fourth column contains the 99.7% confidence interval.

was determined from the distribution of the 10,000 ZDCF peaks (see Section 3.2 of Boyce et al. 2019). In Figure 2, the observed correlation function (black) displays a stronger signal of correlation than the spread of simulations (blue) because of the way the data points in the simulated light curves are chosen. Each data point in a simulated light curve is randomly selected from a Gaussian distribution centered on the observed flux value in that bin with a standard deviation equal to the 1σ errors on the measured data. Therefore, real correlations in the detailed shape of the light curve (e.g., a monotonic rise) may not be strongly reproduced in a given simulated instance. The height of the shaded blue regions above the simulated noise can therefore be seen as a pessimistic indicator of how real the correlation is. Thus, the width of the distribution of peak locations drawn from the simulations can conservatively estimate the uncertainty on the time lag. A positive time lag corresponds to variability in the the NuSTAR, Chandra, GRAVITY, or ALMA data lagging the 4.5 μm Spitzer variability, while a negative time lag corresponds to variability leading 4.5 μm.

Spitzer−NuSTAR. Figure 2 shows the results of running the ZDCF on the 2019 July 18 epoch of the Spitzer data and the 6 minute binned NuSTAR light curve. The measured time lag for the flare plotted in Figure 4 and reported in Table 2 at $+2^{+15}_{-15}$ minutes is consistent with simultaneity but less significant than the Chandra X-ray measurement due to lower signal-to-noise ratio and sensitivity in the data.

Spitzer−Chandra. The second row of Figure 2 shows the results of running the ZDCF on the 2019 July 17/18 epoch of the Spitzer data and 300 s binned Chandra light curve. The measured time lag for the flare plotted in Figure 4 and reported in Table 2 at -3^{+3}_{-3} minutes is consistent with simultaneity.[19]

Spitzer−GRAVITY. The results of running the ZDCF on the 2019 July 17/18 epoch of the Spitzer data against the 40 s binned *K*-band GRAVITY light curve are also shown in Figure 2. The measured time lag for the flare is plotted in orange in Figure 4 and reported in Table 2 at $+0^{+1}_{-3}$ minutes, consistent with simultaneity.

Spitzer−ALMA. Figure 2 shows the results of running the ZDCF on the 2019 July 17/18 epoch of the Spitzer and 340 GHz ALMA light curves, while the cross-correlations of the 2019 July 21 and 26 data sets are plotted in Figure 3. The measured time lags for the variability on each date are plotted in gray in Figure 4 and reported in Table 2.

Only data from July 18 show an X-ray flare with significant simultaneous NIR activity. During this window of 02:30–05:00, ALMA measured significant variability but missed the crucial window of 03:00–03:50 in which the NIR and X-ray flares occurred. The observed peak submillimeter flux occurred around 04:00, right after the window of missing data but at a time when NIR and X-ray flux levels had returned to typical quiescent rates. The result from the ZDCF on the July 18 Spitzer-versus-ALMA data is a measured time lag of $+34^{+2}_{-8}$ minutes at 68% confidence and $+34^{+14}_{-33}$ at 99% confidence. It is therefore likely that the peak of the submillimeter flux lagged the NIR and X-ray variability by tens of minutes, though we must interpret $\sim$35 minutes as an upper limit on the time lag, since the true peak was not observed.

Cross-correlating the Spitzer and ALMA light curves on July 21 and 26 followed the same method, and the results are displayed in Figure 3. Though there was not a significant X-ray flare, the NIR and submillimeter show distinguishable variability. The cross-correlation of July 21 results in a lag of $+27^{+12}_{-58}$ minutes at 68% significance, a broad range that reaches over two marginally significant correlation peaks at around −40 and +40 minutes. The cross-correlation of July 26 results in a lag of $+20 \pm 14$ minutes at 68% significance, consistent with the lag detected on July 18, but is also consistent with simultaneity $\sim$20% of the time. Figure 4 summarizes the results.

4. Discussion

Variability in the NIR has been successfully described by the intermittent acceleration of electrons in a turbulent accretion flow, most often modeled as nonthermal synchrotron emission with a varying cooling cutoff. This is supported by the observed linear polarization of the IR emission (Eckart et al. 2006a; Meyer et al. 2006, 2007; Trippe et al. 2007; Yusef-Zadeh et al. 2007; Eckart et al. 2008a; Witzel et al. 2011; Shahzamanian et al. 2015), the spectral index at high flux densities ($\alpha \approx -0.6$; Hornstein et al. 2007; Bremer et al. 2011; Witzel et al. 2014), and the timescale of the variability, with factors of $\gtrsim$10 changes within $\sim$10 minutes (e.g., Genzel et al. 2003; Ghez et al. 2004; Witzel et al. 2018).

The physical parameters of this turbulent acceleration of electrons (e.g., background magnetic field strength B, the Lorentz factor of the electrons γ, and the electron density n_e) and the details of the radiative processes linking the NIR variability to the X-ray flares are still uncertain. The processes often invoked to make this connection include (1) pure synchrotron from a sudden acceleration of electrons to a nonthermal distribution (e.g., Markoff et al. 2001; Dodds-Eden et al. 2009; Barrière et al. 2014; Ponti et al. 2017), (2) SSC through the scattering of these nonthermal synchrotron photons up to X-ray energies (Markoff et al. 2001; Eckart et al. 2008a, 2012; Witzel et al. 2021), and (3) inverse Compton scattering of radio and submillimeter photons from the

[19] An updated barycenter correction was applied to all reductions of the current and previous Chandra data. This slightly altered the original results from Boyce et al. (2019) but remained within the 1σ uncertainties. The time lags for those NIR/X-ray epochs were recalculated and reported in Boyce et al. (2021), as well as here in Table 2 and Figure B1 in Appendix B.

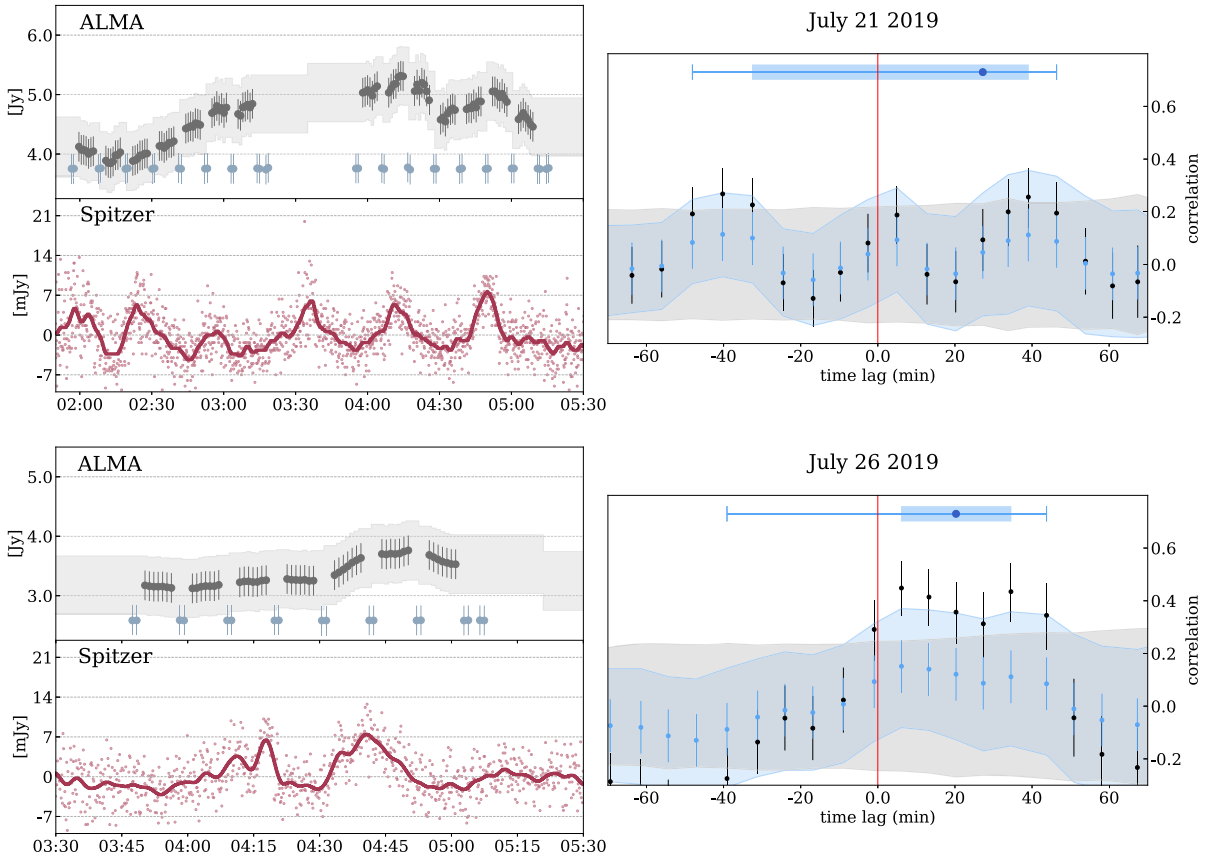

Figure 3. Results from running `ZDCF` on the ALMA (gray) light curves against the respective Spitzer (red) light curves on 2019 July 21 and 26. Left panels: regions of the light-curve portions where we see significant IR activity in the overlapping data. The gray envelopes show the 95% range of the 10,000 MC realizations. The x-axes display the UTC time since the start of the Spitzer/IRAC observations. In the right panels, the blue points are the average cross-correlation of all 10,000 MC realizations, with the blue envelope capturing the 95% range. The gray envelope is the 95% range from the IR MC realizations with 10,000 realizations of simulated noise consistent with the rms of the ALMA light curve's emission (no flares). The significant time lags and confidence intervals are plotted as a single blue point in each panel, with the 68% interval represented by the blue shaded box and the 99.7% interval represented by the thin error bar.

synchrotron source produced by the persistent large population of thermal electrons (Yusef-Zadeh et al. 2012). All of these scenarios can include changes in the source's magnetic field (B), electron density (n_e), and Lorentz factors (γ). The most likely scenario may be some combination of multiple processes, but the unpredictable nature of flares from around accreting BHs limits data collection, and often the best way forward is testing one scenario at a time.

More broadly, Sgr A*'s average SED is described by several varying components that could originate from different zones in the accretion flow. Though the connection between the NIR and X-ray is clear, it remains an open question whether submillimeter variability could originate from the same source as the higher-energy variability. Periods of increased submillimeter variability can be described by separate, uncorrelated events that are occasionally coincident with NIR/X-ray flares. We ask whether the submillimeter, NIR, and X-ray variability on July 18 could be explained through a single acceleration event, i.e., a single zone modeled at the peak of the NIR/X-ray flare and tens of minutes later, when submillimeter flux is observed to be declining from an unknown peak value.

To tackle this question, we reexamine three different scenarios of processes 1 and 2 in light of the total data set from the campaign presented here, wherein (A: 0-SYNC-SYNC) nonthermal emission originating from a single source of accelerated electrons is responsible for the NIR and X-ray while contribution to the submillimeter is negligible, (B: SYNC-SYNC-SSC) nonthermal synchrotron emission is responsible for the submillimeter and NIR while the X-rays are produced through SSC processes, and (C: SYNC-SSC-SSC) submillimeter flux density is due to a nonthermal population of electrons emitting synchrotron radiation while both the NIR and X-ray are dominated by the SSC emission. Inverse Compton (IC) scattering of external thermal submillimeter photons (process 3) is not examined. All SEDs discussed in the following sections are produced with `flaremodel` (Dallilar et al. 2022), a code for numerically modeling one-zone synchrotron sources.[20]

Our multiwavelength time-resolved data constrain the evolution of the source as these electrons cool and/or are continuously accelerated. We are motivated to test these single-zone descriptions because they do not overfit our data by introducing complex geometries and because flaring in the NIR has been successfully described as originating from a compact, orbiting hot spot on horizon scales (Bauböck & Dexter et al. 2020a). Once electrons are accelerated, they may cool via several channels that would affect the accretion structure

[20] Available at https://github.com/ydallilar/flaremodel.

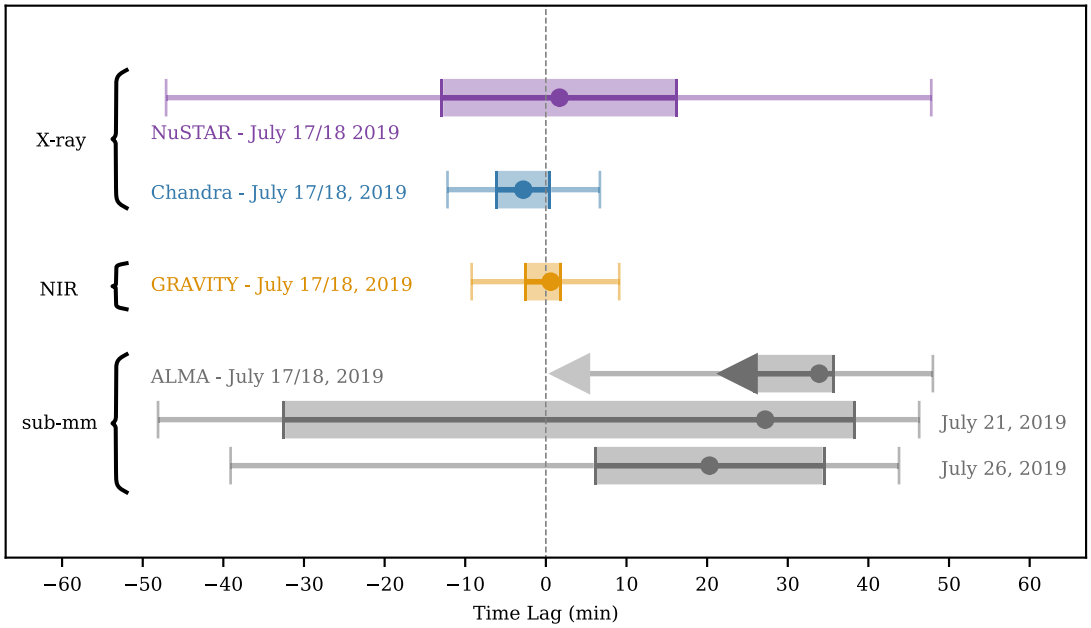

Figure 4. Time lags between all multiwavelength observations and Spitzer 4.5 μm light curves for the Sgr A* 2019 July campaign. The purple, blue, orange, and gray points show the NuSTAR 3–70 keV, Chandra 2–8 keV, GRAVITY *K*-band (2.2 μm), and ALMA 340 GHz lags, respectively. The 68% confidence intervals are represented by the shaded boxes, and the 99.7% intervals are represented by the thin error bars. Because the measured submillimeter lag on July 18 is an upper limit, the peak of the flare was not captured.

around a BH (e.g., synchrotron, bremsstrahlung, and inverse Compton processes; Yoon et al. 2020). Here we examine one possibility via cooling under adiabatic expansion, in which a uniform and spherical cloud of relativistic electrons is expanding and the cooling applies to electrons of all energies at the same rate set by the expansion speed. We refer to the time of the NIR/X-ray peak as $t = 0$ and the time of the measured 340 GHz peak as $t = 35$ minutes.

4.1. (A) +SYNC+SYNC: An Evolving Synchrotron Source

We consider the scenario where both the NIR and X-ray are produced by a single synchrotron spectrum originating from particle acceleration events involving magnetic reconnection and shocks in the accretion flow (e.g., Markoff et al. 2001; Dodds-Eden et al. 2009; Barrière et al. 2014; Ponti et al. 2017; Rowan et al. 2017). An example of this scenario is plotted as the dashed line in Figure 5. With both bands being produced by a single nonthermal synchrotron source, the synchrotron cooling time in the NIR would far exceed the X-rays, and the source would require sustained particle acceleration to produce observed X-ray flare durations of up to ∼1 hr. In this scenario, rapid synchrotron cooling will cause fading in the higher-energy X-rays sooner than in the NIR (e.g., see Section 4.1 of Dodds-Eden et al. 2010). This could manifest as a simultaneous rise with a time delay between the X-ray and NIR flare "centers" of a few to tens of minutes if the time resolution and signal-to-noise ratio of our observed X-ray light curves were high enough (Dodds-Eden et al. 2010).

Cooling the best-fit synchrotron model of Abuter et al. (2021) at time $t = 0$ (via any cooling process) would result in a decrease in flux across the SED and would not produce appreciable flux in the submillimeter. Therefore, if the NIR and X-ray variability is due to a purely SYNC component (see, e.g., Ponti et al. 2017), that same source could not explain the observed ∼2 Jy increase in flux density at 340 GHz. The variability at these wavelength regimes must be physically uncorrelated or involve more

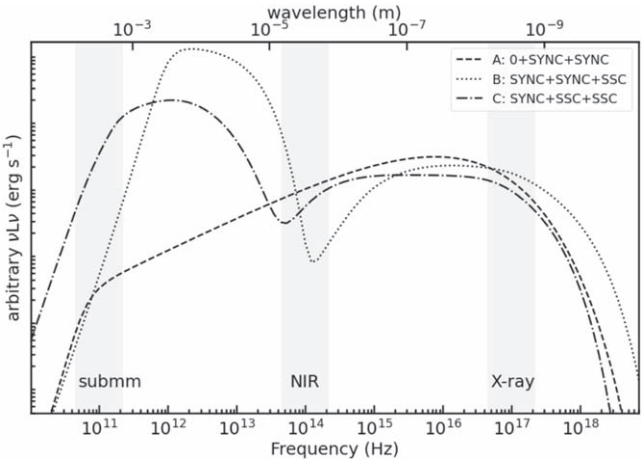

Figure 5. Illustration of the three example SED models at the time of the NIR/X-ray peak ($t = 0$). (A) The dashed line represents model 0-SYNC-SYNC, in which both the NIR and X-ray flux are described by a synchrotron source that contributes negligibly to the submillimeter. (B) The dotted line represents model SYNC-SYNC-SSC, in which the optically thick cutoff of the nonthermal SYNC component contributes to the submillimeter, the varying optically thin cutoff of the same SYNC component contributes to the NIR, and the X-ray variability is produced through SSC. (C) The dashed–dotted line represents model SYNC-SSC-SSC, in which submillimeter flux can be explained through the optically thick SYNC, NIR flux is dominated by SSC, and the X-rays are also produced by SSC. The models illustrate the shape of the SEDs, but the relative vertical position (flux) of these example curves is arbitrary. The details are described in Dallilar et al. (2022).

complex models containing multiple zones of accelerated electrons in complex geometries. On the other hand, more complex models or geometries are difficult to include in the scenario wherein the submillimeter flux correlates with NIR flares originating from a compact orbiting hot spot on horizon scales (Bauböck & Dexter et al. 2020a).

In summary, the best-fit cooled SYNC model described in Abuter et al. (2021) accounts for the X-ray and NIR variability

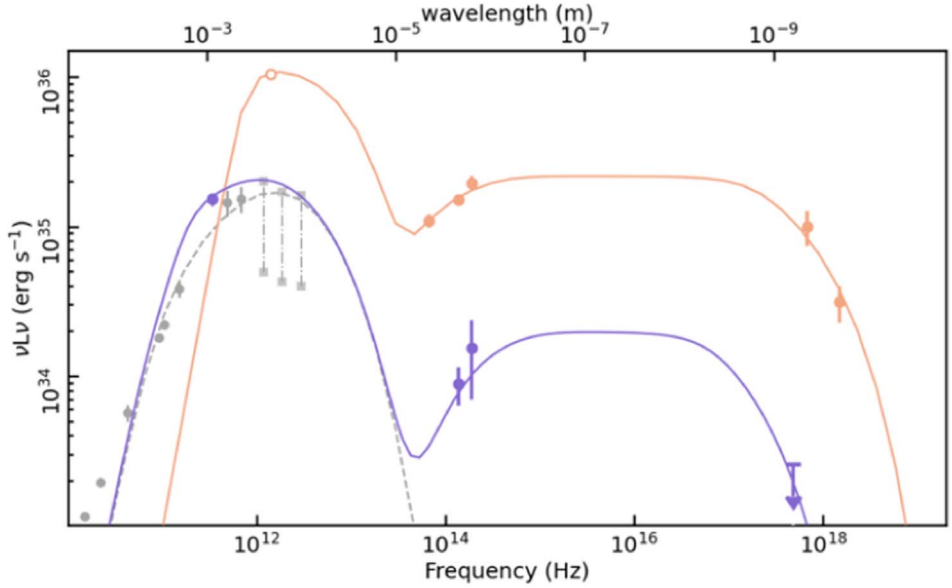

Figure 6. Snapshots of the time evolution of scenario (C) SYNC-SSC-SSC, fit under adiabatic expansion. Filled orange points are measured values at the peak of the NIR and X-ray flare, and purple points are measured at the presumed "peak" of the 340 GHz flux ∼35 minutes later. The open orange point at 1400 GHz is used as the starting point in the adiabatic expansion calculation described below. The historic quiescent SED in the radio/submillimeter is plotted in gray, with a thermal synchrotron component fit to these data as the gray dashed line. The solid lines are the best-fit models with the thermal component included. Parameters for the fits are reported in Table 3. Observed values are tabulated in Table A1.

and does not require unusually large electron densities. However, as this synchrotron source cools, flux at all wavelengths decreases. A simultaneous or delayed 1–2 Jy increase in the submillimeter flux density requires invoking multiple nonthermal populations of accelerated electrons and would not be physically correlated through the evolution of the same SYNC source responsible for the NIR and X-rays.

4.2. (B) SYNC+SYNC+SSC: An Adiabatically Cooling Synchrotron Source

Witzel et al. (2021) considered a simple physical model of a compact synchrotron component in Sgr A*'s accretion flow undergoing a sequence of

1. injection of nonthermal electrons giving rise to detectable submillimeter and NIR emission;
2. further injection, compression of the source, and increasing magnetic flux resulting in higher NIR levels and detectable X-ray emission; and
3. adiabatic expansion with little to no injection giving rise to maximum submillimeter emission. (For a deeper description, see Section 4 of Witzel et al. 2021, along with their Figure 11.)

This sequence is based on the scenario that there exists a variable synchrotron spectrum arising from populations of nonthermal (accelerated) electrons in addition to the dominant thermal synchrotron radio component of Sgr A*'s SED. The NIR variability is then primarily due to the rapidly varying cooling cutoff of this spectrum. Correlated X-ray variability arises from the resulting SSC spectrum (with the high temporal frequency variability suppressed). This "slow" variability in the SSC X-rays is therefore related to physical changes in the synchrotron source itself (i.e., source size θ, magnetic flux B, and self-absorption properties that manifest in changes to the location of the peak flux and self-absorption frequency turnover of the synchrotron spectrum at submillimeter wavelengths). Delayed submillimeter variability relative to the NIR/X-ray is attributed to these physical changes in the source (e.g., cooling causes the SYNC component to shift to longer wavelengths).

This model predicts a delay in peak submillimeter flux density on the order of 20–30 minutes, consistent with our upper limit of ∼35 minutes. It also describes the correlation of the majority of NIR and X-ray flares in the literature. Michail et al. (2021) considered an analogous description of the synchrotron source for the case that the 2018 July 18 NIR and submillimeter emission were simultaneous and found that conditions with $p = 2.5$ describe the submillimeter/IR flux increase well. In this case, simultaneity in the submillimeter and NIR could occur if conditions in the accretion flow produced a SYNC source with optically thin emission reaching from the submillimeter regime to the NIR. This is incompatible with our observations in two ways. First, the SYNC spectrum whose peak is near 340 GHz and broadly reaches the NIR does not produce SSC in the correct regime to fit the NIR/X-ray data. Second, this SYNC spectrum rising in the submillimeter and reaching the NIR would not have the spectral index observed in the IR.

For typical ranges of physical parameters, most of the variable NIR flux is produced by the optically thin cutoff of the synchrotron component and described by relatively steep flux spectral index ($F_\nu \propto \nu^\alpha$) in the range $-2.0 \lesssim \alpha \lesssim -0.8$, resulting in a negative or flat luminosity spectral index ($\beta = \alpha + 1$). An example of this model (with a steep negative spectral index) is plotted as the dotted line in Figure 5.

Abuter et al. (2021) measured the evolution of the NIR spectral index of the July 18 flare and found that the GRAVITY K-band to Spitzer M-band slope varied in the range $\alpha_{K-M} = [-0.8, 0.0]$, consistent with the canonical NIR spectral index for bright flares of $\alpha_{\rm NIR} \sim -0.65$ (Eisenhauer et al. 2005; Ghez et al. 2005; Gillessen et al. 2006; Krabbe et al. 2006; Hornstein et al. 2007; Bremer et al. 2011; Witzel et al. 2014; i.e., luminosity rising with shorter wavelengths). This is reflected in Figure 6, where the orange points in the NIR band

have positive β. Since this flare has an NIR spectral index $\alpha \sim -0.6$ at its peak (Figure 6), we favor descriptions with positive luminosity photon indices ($\nu L_\nu \propto \nu^\beta$, $\beta = \alpha + 1$).

In summary, though this scenario could explain the temporal evolution of the correlated submillimeter, NIR, and X-ray flux densities, the spectral index in the NIR disfavors a scenario in which the NIR is dominated by the optically thin component of the SYNC spectrum.

4.3. (C) SYNC+SSC+SSC: An Adiabatically Cooling Synchrotron Source

Another possibility is that both the X-ray and NIR flux may be dominated by SSC flux (i.e., photons being scattered to higher energies through interaction with the electrons producing the nonthermal synchrotron in the submillimeter). In this scenario, the NIR flux would derive from the rising side of the SSC component, rather than the optically thin edge of the SYNC component (which is now shifted toward even longer wavelengths). An example of this SED is illustrated as the dashed–dotted line in Figure 5.

Since the SYNC+SSC+SSC scenario predicts the correct range of NIR spectral indices, we fit this model with a synchrotron source that produces the 340 GHz flux increase that can evolve under adiabatic expansion. If adiabatic cooling is dominant, the SYNC source expands and cools (without further electron injection), causing the turnover of the SYNC component to march down to a lower frequency as it fades. This results in a delay at longer wavelengths. If the true peak of the submillimeter rise was simultaneous with the NIR/X-ray, the SYNC component of the SED must have peaked near 340 GHz. Such a SYNC spectrum could not then produce bright enough SSC emission to match the NIR/X-ray observations. We therefore consider the scenario in which the peak of the submillimeter emission was delayed by tens of minutes.

To test this scenario and leverage the submillimeter flux measured with a delay, we use the methodology first described in van der Laan (1966) to parameterize the behavior of the peak of the nonthermal SYNC component under adiabatic cooling. This method has been applied to interpret Sgr A* variability in the past (e.g., Yusef-Zadeh et al. 2006a; Eckart et al. 2008b).

The flux density as a function of frequency (ν) is parameterized as

$$S(\nu, \rho) = (\nu/\nu_m)^{5/2}\rho^3 \times \frac{\left[1 - \exp\left\{-\tau_m\left(\frac{\nu}{\nu_m}\right)^{-(p+4)/2}\rho^{-(2p+3)}\right\}\right]}{[1 - \exp(-\tau_m)]}, \quad (1)$$

where ν_m is the frequency at which the flux density maximum of the spectrum occurs, p is the slope of the electron distribution, τ_m is the optical depth corresponding to the frequency at which the flux density is maximum, and ρ is the relative radius of the source, which can be parameterized in terms of the expansion velocity $v_{\rm exp}$, time (t), initial source size R_0, and a deceleration parameter β (kept at a standard value of 1.0 in our analyses):

$$\rho = \left(\frac{1 + v_{\rm exp}\, c(t - t_0)}{R_0 \beta}\right)^\beta. \quad (2)$$

To describe the broadband SED, we numerically implement the SYNC-SSC model described in Dallilar et al. (2022), based on a nonthermal power law–distributed electron energy distribution. The physical parameters of this single-zone nonthermal synchrotron model are the electron density ($n_e \times 1$ cm^3), projected radius (R, μas), magnetic field (B, G), power-law slope of the electron distribution (p), maximum Lorentz factor ($\gamma_{\rm max}$), and minimum Lorentz factor ($\gamma_{\rm min}$).

Table 3
Best-fit Parameters of Scenario C: SYNC+SSC+SSC

	$t = 0$	$t = 35$ minutes
log ($n_e \times 1$ cm^{-3})	10.1 ± 0.8	9[b]
R (μas)[a]	11.2 ± 2.1	21 ± 2
B (G)	25 ± 44	3.1 ± 0.8
p	3[b]	3[b]
$\gamma_{\rm max}$	320 ± 110	410 ± 130
$\gamma_{\rm min}$	3.8 ± 1.3	10.8 ± 3.4
$\chi^2_{\rm red}$	2.3	0.5

Notes.
[a] 1 μas = 0.0082 au.
[b] Value fixed.

Plotted in orange in Figure 6 are the observed X-ray and NIR data at the time of their peak ($t = 0$). Due to the gap in the observing window, we do not have a simultaneous measurement at 340 GHz. However, under the assumption that there is a significant time lag of ~35 minutes or less in the peak of the submillimeter flux, the 340 GHz flux at $t = 0$ must be fainter than ~2 Jy (excess flux above historic quiescence; 5.5×10^{34} erg s^{-1} at 340 GHz). The orange line is the best-fit SSC-SSC SED that satisfies this constraint with $\chi^2_{\rm red}$ of 2.3. Experimenting with the errors on the data, we find that the high H-band measurement prevents the fit from reaching $\chi^2_{\rm red} \sim 1$. Doubling the uncertainty on this point would result in $\chi^2_{\rm red} = 1.1$ with very similar values to those listed in Table 3.

In purple are the constraints in the NIR/X-ray once their flux has faded (at 35 minutes past peak), as well as the measured "peak" flux at 340 GHz. Fitting these data with the SYNC +SSC+SSC SED and the SYNC thermal component (gray) yields $\chi^2_{\rm red}$ 0.5. The physical parameters of these best fits are tabulated in Table 3.

Taking the best-fit radius at $t = 0$ ($R_0 \sim 1.1 \times R_{\rm S}$) and the peak flux at 1400 GHz (10.8 − 1.5 = 9.3 Jy after subtracting the thermal component from the peak in Figure 6), we apply Equations (1) and (2) (van der Laan 1966) to match the peak flux in 340 GHz at $t = 35$ minutes. With the initial size of the region, R_0, set at the best-fit value, we can vary the expansion speed and find that a value of $v_{\rm exp} \sim 0.014c$ reproduces the flux observed at the peak in 340 GHz (see Figure 7). This speed is consistent with other estimates of $v_{\rm exp} \sim 0.003c$–$0.02c$ found under the interpretation of an expanding plasmon (Yusef-Zadeh et al. 2006a, in the centimeter; and Eckart et al. 2006b, 2008b; Marrone et al. 2008; Eckart et al. 2012, in the NIR–submillimeter). This calculation relies on the assumption that the peak in 340 GHz occurred at $t = 35$ minutes. If the peak happened earlier, we would require an even faster expansion speed to match the measured flux.

Scenario C (SYNC+SSC+SSC) can be interpreted as a particularly unusual version of scenario B, in which the same single-zone model and radiation mechanisms could produce typical flux variations in the submillimeter, NIR, and X-ray. In this picture, the July 18 event's unusually high submillimeter

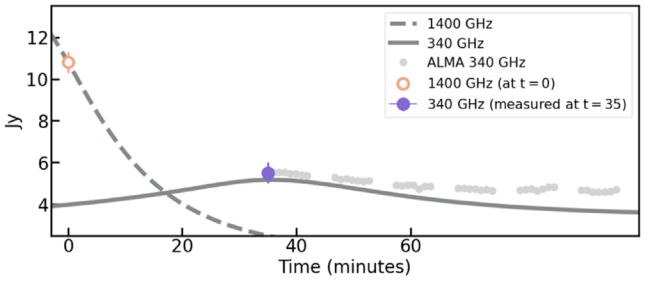

Figure 7. Light curves derived from Equations (1) and (2) offset with the constant flux values originating from the putative constant synchrotron component that arises from a thermal distribution of electrons (gray dashed line in Figure 6; 1.5 Jy at 1400 GHz and 3.4 Jy at 340 GHz). A value of 9.3 Jy at 1.4 THz (10.8 Jy from Figure 6; 1.5 Jy from the thermal component) is used in the calculation and evolved forward in time with expansion velocity $v_{exp} = 0.014c$. The purple data point (5.5 Jy) is the measured 340 GHz flux with the thermal synchrotron component (3.4 Jy) included.

flux is explained through uniquely high electron densities and a prediction of bright emission in the THz regime.

This interpretation relies on the validity of two unique characteristics. First, there must have been very high flux at ∼THz frequencies during the flare, something that has not been reported in campaigns aiming to characterize the quiescent THz spectrum (von Fellenberg et al. 2018; Bower et al. 2019), though at 850 GHz, Serabyn et al. (1997) reported a measurement of ∼3 Jy (2×10^{35} erg s^{-1}). An updated study of the flux density distribution at submillimeter–THz is required to determine the likelihood of observing such a flare based on past observations at these frequencies. Second, electron densities in the SYNC source must have been several orders of magnitude higher than the implied densities of the average accretion flow from radio polarization studies ($\log n_e \sim 10$ compared to, e.g., ∼7; Bower et al. 2019), which could be easier to achieve if Sgr A* were in an unusual state of increased accretion.

Average accretion rates for Sgr A* are estimated from the rotation measure in quiescent submillimeter observations, the last of which was Bower et al. (2018), based on data obtained in 2016. The rotation measure has been observed to have short-term variability, and most estimates of Sgr A*'s accretion rate are cited from the value averaged over the long term (∼years). Since then, there have been hints that Sgr A*'s accretion state may not be so constant, particularly supported by the incredibly bright NIR flare observed in early 2019 (Do et al. 2019), which fell outside of all previously parameterized flux density distributions. If Sgr A* was indeed in a state of elevated accretion in 2019, then this could explain how this event is distinct from most previously observed flares. That is, a high sub-THz flux may be more easily achievable if electron densities as a whole are increased, allowing flaring conditions with $\log n_e \sim 10$.

Finally, the assumption that we have captured the peak of the 340 GHz flare is a large one. The start of the observing window around 03:45 catches the light curve in a descending state, with no indication of a turnover (Figure 1). If we have not captured the peak of the flare, that will allow the SYNC component in this SED to extend to lower energies at the time of the NIR/X-ray peak, though it will still remain significantly higher than the previously observed flux levels at these frequencies.

Fitting the temporally resolved SED over six time steps in the NIR and X-ray, Abuter et al. (2021) concluded that the particle densities necessary for SYNC+SSC+SSC ($\gg 10^9$ cm^{-3}) would be extremely unlikely given the typical average electron densities derived from modeling the radio-to-submillimeter SED of Sgr A* with synchrotron emission from a thermal electron distribution (ambient $n_e < 10^7$ cm^{-3}; Bower et al. 2019). To fit an SED like A (0+SYNC+SYNC), a strong acceleration event is necessary ($\gamma_{max} \gg 10^4$), but the physical parameters of the source (including n_e) remain consistent with predictions from the literature.

Of course, adiabatic expansion is not the only scenario in which delayed and correlated emission between frequencies can arise. Interpreting 20–40 minute delays in the 20–40 GHz regime, Falcke et al. (2009) observed a frequency dependence of very long baseline interferometry sizes and saw evidence for a relativistic outflow. Meanwhile, Brinkerink et al. (2015) derived relativistic outflow velocities of up to $\sim 0.77c$ through the progression of variability maxima from 100 to 19 GHz and interpreted this as a jet. Finally, it is always possible that the submillimeter variability is not physically correlated with the NIR and arises from another component altogether. For example, single-zone modeling of M87's jet and active galactic nucleus cannot fully describe the broadband SED, albeit the data most driving this conclusion are the high-energy γ-rays (EHT MWL Science Working Group et al. 2021).

In summary, this single-zone adiabatic expansion model fits the data, with the caveat that the inferred submillimeter–THz flux at $t = 0$ would have been much brighter than most observations at these frequencies. Accepting the plausibility of the scenario requires an electron density that would be extraordinarily high in comparison with the estimated densities responsible for Sgr A*'s average accretion rate.

5. Summary

We report observations from a multiwavelength campaign that simultaneously observed Sgr A* in 2019 July from the submillimeter to NIR to X-ray. Cross-correlating the light curves against the Spitzer NIR light curve on each date, we report the measured time lags between each wavelength.

1. On July 17−18, a moderately bright NIR flare captured by Spitzer (4.5 μm) and GRAVITY (2.2 μm) occurred simultaneously with a faint X-ray flare captured by NuSTAR (3–70 keV) and Chandra (2–8 keV). Overlapping coverage at 340 GHz from ALMA missed the peak of the submillimeter flare but reveals very bright correlated flux ∼35 minutes after the NIR/X-ray peak.
2. On July 21, correlated submillimeter/NIR flux variability remains consistent with simultaneity (no time lag).
3. On July 26, we report a measured time lag of ∼20 minutes between correlated submillimeter and NIR variability with 68% confidence but consistent with simultaneity at 98% confidence.

The flux and timing properties of the July 17−18 flare are considered in the context of three scenarios: (A) both NIR and X-ray due to emission from a synchrotron source, (B) submillimeter and NIR due to a synchrotron source while X-ray arises as synchrotron self-Compton emission, and (C) submillimeter due to a synchrotron source while both NIR/X-ray arise from synchrotron self-Compton. We are limited in what we constrain because we have not captured the peak of the 340 GHz flare and can only measure an upper limit on the time lag between it and the NIR. This event is particularly interesting because the submm flux is notably high (∼5.5 Jy,

very rarely observed at these frequencies), so if the peak is even higher, this could indicate that the radiative processes are non-typical when compared to conditions responsible for historic variability. In the scenario in which the submm and NIR/X-ray variability are not physically correlated, a SYNC source fitted to the NIR/X-ray (scenario "A") is allowed and does not require extraordinarily large electron densities (Abuter et al 2021).

To leverage the potentially delayed submillimeter flux, we consider whether a synchrotron source cooled through adiabatic expansion can self-consistently describe the sub-millimter increase and the NIR/X-ray flux at peak and after. Consistent with our measurement, Michail et al. (2021) reported an upper limit on the time lag of less than 30 minutes. They also analyzed the submillimeter and mid-IR emission using adiabatically expanding synchrotron plasma models and found two cases can describe the data. The first is a SYNC source with $p = 2.5$ responsible for a simultaneous rise in the submillimeter and NIR (analogous to scenario B SYNC +SYNC+SSC). We disfavor this scenario primarily because the predicted NIR spectral index is in tension with the observations but also because a simultaneous rise in the submillimeter and NIR would require a SYNC spectrum whose peak is near 340 GHz and broadly reaches the NIR, which does not produce SSC in the correct regime to fit the X-ray data. In their second case, a SYNC source with $p > 2.8$ has optically thick plasma conditions that evolve to optically thin in the submillimeter on the timescale of tens of minutes (analogous to scenario C SYNC+SSC+SSC). We find that this adiabatic expansion scenario producing SSC emission in the NIR and X-rays (scenario C) works only under the conditions that a very high submillimeter/THz peak would occur at the time of the NIR/X-ray peak and that the electron density reaches $\log n_e \sim 10$.

Narrowing down the radiation mechanism powering and connecting variability across wavelength regimes brings the field closer to accurately describing the physical mechanisms that power the dramatic flux changes originating near the event horizon. Simultaneous multiwavelength observations of Sgr A* at all accessible frequencies remain essential to differentiate between various radiation mechanisms. Such observational campaigns are key to comparing to the state-of-the-art GRMHD simulations that can model details of accreting plasma in this extreme environment, where high-resolution simulations have shown that sufficiently energetic plasma can be accelerated through magnetic reconnection (Ripperda et al. 2022). In particular, continued coordination between submillimeter–radio observatories and the NIR/X-ray will strengthen or rule out the interpretation that these variable signals are physically connected. If simultaneous observations at THz frequencies are also captured during submillimeter/NIR/X-ray variability, one could definitively constrain models in which the cooling SYNC component is responsible for the sub-millimeter flux density increase and correlated with NIR/X-ray SSC emission. Finally, coordinated multiwavelength campaigns with the EHT and VLTI/GRAVITY will be key to interpreting the increasingly detailed view of this accreting SMBH on horizon scales.

We thank the GRAVITY collaboration for sharing the flux data for July 17/18 (Abuter et al. 2021) and their valuable feedback on the analysis and text. We are grateful to Yigit Dallilar for help in the utilization of the `flaremodel` SED code (Dallilar et al. 2022), his expert guidance in the implementation of adiabatic expansion codes, and numerous fruitful scientific discussions. We are thankful for Gabriele Ponti's helpful input and insightful discussions. We thank Eduardo Ros for his careful reading of the text and valuable clarifying comments. The authors are grateful for access to the privileged location of the high-altitude plateau Chajnantor in the land of the indigenous Likanantai people on which the ALMA telescope sits. H.B. and D.H. acknowledge and thank the diverse indigenous people on whose land our home institutions reside in Tiohti:áke, including the Haudenosaunee and Anishinabeg peoples and the Kanien'kehá:ka Nation. The authors thank the anonymous referee for constructive comments and insight. H.B. is grateful for support from the Natural Sciences and Engineering Research Council of Canada (NSERC) Alexander Graham Bell Canada Graduate Scholarship. H.B. and D.H. acknowledge funding from the NSERC Discovery Grant and the Canada Research Chairs (CRC) program. The scientific results reported in this article are based on observations made by the Chandra X-ray Observatory, the Spitzer Space Telescope, the Nuclear Spectroscopic Telescope Array (NuSTAR), the GRAVITY instrument on the Very Large Telescope, and the Atacama Large Millimeter/submillimeter Array (ALMA). This paper makes use of the following ALMA data: ADS/JAO.ALMA#2018.A.00050.T. ALMA is a partnership of ESO (representing its member states), NSF (USA) and NINS (Japan), together with NRC (Canada), MOST and ASIAA (Taiwan), and KASI (Republic of Korea), in cooperation with the Republic of Chile. The Joint ALMA Observatory is operated by ESO, AUI/NRAO and NAOJ. The National Radio Astronomy Observatory is a facility of the National Science Foundation operated under cooperative agreement by Associated Universities, Inc. We thank the Chandra, Spitzer, NuSTAR, ALMA, and GRAVITY scheduling, data processing, and archive teams for making these observations possible.

Facilities: Spitzer/IRAC, Chandra/ACIS, NuSTAR, VLTI/GRAVITY, ALMA.

Software: `CIAO` (Fruscione et al. 2006), `NumPy` (Jones et al. 2001), `AstroPy` (The Astropy Collaboration et al. 2018), `matplotlib` (Hunter 2007), `bayesian blocks` (Williams et al. 2017), `zdcf` (Alexander 2013), `flaremodel` (Dallilar et al. 2022).

Appendix A
SED Values

Table A1 reports the values for Sgr A*'s SED that correspond to Figure 6.

Table A1
Values for the Sgr A* SED Observed by Coordinated Ground- and Space-based Observatories on 2019 July 18

Observatory	Frequency [GHz]	$t = 0$ minutes		$t = 35$ minutes	
		Flux Density [Jy]	νL_ν [$\times 10^{34}$ erg s^{-1}]	Flux Density [Jy]	νL_ν [$\times 10^{34}$ erg s^{-1}]
ALMA[a]	340	⋯	⋯	2.6 ± 0.5	7.2 ± 1.4
Spitzer/*M*-band	6.7×10^4	$20.2 \pm 1.0 \times 10^{-3}$	10.9 ± 0.6	⋯	⋯
GRAVITY/*K*-band	1.4×10^5	$13.5 \pm 0.9 \times 10^{-3}$	15.0 ± 1.0	$0.8 \pm 0.2 \times 10^{-3}$	0.9 ± 0.3
GRAVITY/*H*-band	1.9×10^5	$12.7 \pm 1.4 \times 10^{-3}$	19.4 ± 2.2	$1.0 \pm 0.5 \times 10^{-3}$	1.5 ± 0.8
Chandra	6.8×10^8	$18.1 \pm 4.7 \times 10^{-7}$	10.0 ± 2.6	$<7 \times 10^{-9}$	<0.3
NuSTAR	1.5×10^9	$2.6 \pm 0.7 \times 10^{-7}$	3.1 ± 0.9	⋯	⋯

Note. Frequencies for X-ray observatories reflect the central frequency of the keV energy band within the observation bin.
[a] After subtracting the ∼2 Jy contribution from the thermal component (gray line in Figure 6).

Appendix B
Comparison with Previous NIR/X-Ray Studies

Several other works have reported simultaneous X-ray and IR observations of Sgr A*. Some report simultaneity between the X-ray and IR peaks but do not report a time frame within which that claim can be considered valid (Yusef-Zadeh et al. 2006b, 2009; Trap et al. 2011). Those that constrain timing between X-ray and IR activity (Eckart et al. 2004, 2006b; Hornstein et al. 2007; Eckart et al. 2008a; Dodds-Eden et al. 2009; Eckart et al. 2012; Ponti et al. 2017; Hornstein et al. 2007; Yusef-Zadeh et al. 2012) are plotted in Figure B1 along with the Spitzer–Chandra results of this campaign. Table B2 reports all updated time lags measured from the Spitzer–Chandra campaign.

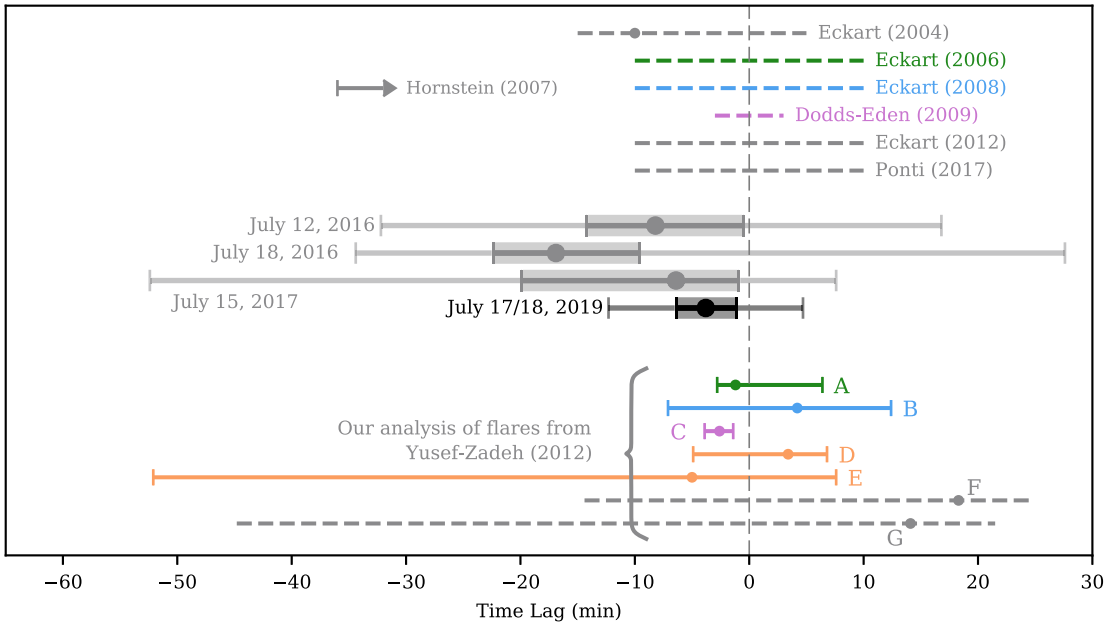

Figure B1. Time lags between IR and X-ray flares as reported in this work and the literature. Plotted with black circles are the time lags from the epochs in this Spitzer/Chandra campaign with significant X-ray and IR activity and their 68% confidence intervals. Plotted in gray are the updated results from reanalyzing the data in Boyce et al. (2019). Regions marked with dashed lines come from works that describe the flares to be "simultaneous to within *x* minutes" but quote no uncertainties (Eckart et al. 2004, 2006b; Hornstein et al. 2007; Eckart et al. 2008a; Dodds-Eden et al. 2009; Eckart et al. 2012; Ponti et al. 2017). The upper limit from Hornstein et al. (2007) indicates an X-ray flare whose peak occurred 36 minutes before IR observations began. Yusef-Zadeh et al. (2012) is the only work to report any correlation between the X-ray and IR with error bars. Boyce et al. (2019) reanalyzed the seven flares presented in their work, and we plot those results with 68% confidence intervals here. Five of these flares come from previously reported data sets (color coded as green, blue, magenta, and orange for Eckart et al. 2006b, 2008a, Dodds-Eden et al. 2009, and Yusef-Zadeh et al. 2009, respectively), and two come from a previously unreported data set (plotted in gray).

Table B2
Time Lags: Spitzer/Chandra Flares

Date	Time Lag (minutes)	68% Interval	99.7% Interval
2016 July 12	$-13.5^{+5.2}_{-5.1}$	(−18.6, −8.3)	(−29.8, +2.8)
2016 July 18	$-14.4^{+20.4}_{-5.1}$	(−19.5, +6.0)	(−27.5, +18.6)
2017 July 15	$-10.9^{+3.7}_{-4.8}$	(−15.7, −7.2)	(−52.1, +0.4)
2019 July 18[a]	$-2.8^{+3.3}_{-3.3}$	(−6.1, +0.5)	(−12.2, +6.7)

Notes. Negative values mean that X-ray leads IR. Uncertainties on the time lag in the second column span the 68% confidence interval on the 10,000 MC runs. The third column displays the boundaries of this 68% confidence interval, while the fourth column displays the 99.7% confidence interval.
[a] This work.

ORCID iDs

H. Boyce https://orcid.org/0000-0002-6530-5783
D. Haggard https://orcid.org/0000-0001-6803-2138
G. Witzel https://orcid.org/0000-0003-2618-797X
S. von Fellenberg https://orcid.org/0000-0002-9156-2249
S. P. Willner https://orcid.org/0000-0002-9895-5758
T. Do https://orcid.org/0000-0001-9554-6062
A. Eckart https://orcid.org/0000-0001-6049-3132
G. G. Fazio https://orcid.org/0000-0002-0670-0708
M. A. Gurwell https://orcid.org/0000-0003-0685-3621
J. L. Hora https://orcid.org/0000-0002-5599-4650
S. Markoff https://orcid.org/0000-0001-9564-0876
M. R. Morris https://orcid.org/0000-0002-6753-2066
J. Neilsen https://orcid.org/0000-0002-8247-786X
M. Nowak https://orcid.org/0000-0001-6923-1315
H. A. Smith https://orcid.org/0000-0001-6923-1315
S. Zhang https://orcid.org/0000-0002-2967-790X

References

Abuter, R., Amorim, A., Bauböck, M., et al. 2021, A&A, 654, A22
Alexander, T. 1997, in Astronomical Time Series, ed. D. Maoz, A. Sternberg, & E. M. Leibowitz, Vol. 218 (Dordrecht: Kluwer), 163
Alexander, T. 2013, arXiv:1302.1508
Andrés, A., van den Eijnden, J., Degenaar, N., et al. 2022, MNRAS, 510, 2851
Baganoff, F. K., Bautz, M. W., Brandt, W. N., et al. 2001, Natur, 413, 45
Baganoff, F. K., Maeda, Y., Morris, M., et al. 2003, ApJ, 591, 891
Ball, D., Özel, F., Psaltis, D., & Chan, C.-K. 2016, ApJ, 826, 77
Barrière, N. M., Tomsick, J. A., Baganoff, F. K., et al. 2014, ApJ, 786, 46
Boehle, A., Ghez, A. M., Schödel, R., et al. 2016, ApJ, 830, 17
Bower, G. C., Broderick, A., Dexter, J., et al. 2018, ApJ, 868, 101
Bower, G. C., Deller, A., Demorest, P., et al. 2015, ApJ, 798, 120
Bower, G. C., Dexter, J., Asada, K., et al. 2019, ApJL, 881, L2
Boyce, H., Haggard, D., Witzel, G., et al. 2019, ApJ, 871, 161
Boyce, H., Haggard, D., Witzel, G., et al. 2021, ApJ, 912, 168
Bremer, M., Witzel, G., Eckart, A., et al. 2011, AAP, 532, A26
Brinkerink, C. D., Falcke, H., Law, C. J., et al. 2015, A&A, 576, A41
Brinkerink, C., Falcke, H., Brunthaler, A., & Law, C. 2021, arXiv:2107.13402
Čadež, A., Calvani, M., & Kostić, U. 2008, AAP, 487, 527
Capellupo, D. M., Haggard, D., Choux, N., et al. 2017, ApJ, 845, 35
Chan, C.-k., Psaltis, D., Özel, F., et al. 2015, ApJ, 812, 103
Chatterjee, K., Markoff, S., Neilsen, J., et al. 2021, MNRAS, 507, 5281
Chen, Z., Gallego-Cano, E., Do, T., et al. 2019, ApJL, 882, L28
Coti Zelati, F., Rea, N., Papitto, A., et al. 2015, MNRAS, 449, 2685
Coti Zelati, F., Rea, N., Turolla, R., et al. 2017, MNRAS, 471, 1819
Dallilar, Y., von Fellenberg, S., Bauboeck, M., et al. 2022, A&A, 658, A111
Dexter, J., Agol, E., & Fragile, P. C. 2009, ApJL, 703, L142
Dexter, J., Deller, A., Bower, G. C., et al. 2017, MNRAS, 471, 3563
Dexter, J., Kelly, B., Bower, G. C., et al. 2014, MNRAS, 442, 2797
Do, T., Ghez, A. M., Morris, M. R., et al. 2009, ApJ, 691, 1021
Do, T., Witzel, G., Gautam, A. K., et al. 2019, ApJL, 882, L27
Dodds-Eden, K., Gillessen, S., Fritz, T. K., et al. 2011, ApJ, 728, 37
Dodds-Eden, K., Porquet, D., Trap, G., et al. 2009, ApJ, 698, 676
Dodds-Eden, K., Sharma, P., Quataert, E., et al. 2010, ApJ, 725, 450
Eatough, R. P., Falcke, H., Karuppusamy, R., et al. 2013, Natur, 501, 391
Eckart, A., Baganoff, F. K., Morris, M., et al. 2004, AAP, 427, 1
Eckart, A., Baganoff, F. K., Schödel, R., et al. 2006b, AAP, 450, 535
Eckart, A., Baganoff, F. K., Zamaninasab, M., et al. 2008a, AAP, 479, 625

Eckart, A., García-Marín, M., Vogel, S. N., et al. 2012, AAP, 537, A52
Eckart, A., Schödel, R., García-Marín, M., et al. 2008b, AAP, 492, 337
Eckart, A., Schödel, R., Meyer, L., et al. 2006a, AAP, 455, 1
EHT MWL Science Working Group, Algaba, J. C., Anczarski, J., et al. 2021, ApJL, 911, L11
Eisenhauer, F., Genzel, R., Alexander, T., et al. 2005, ApJ, 628, 246
Falcke, H., Markoff, S., & Bower, G. C. 2009, A&A, 496, 77
Fazio, G. G., Hora, J. L., Allen, L. E., et al. 2004, ApJS, 154, 10
Fazio, G. G., Hora, J. L., Witzel, G., et al. 2018, ApJ, 864, 58
Fritz, T. K., Gillessen, S., Dodds-Eden, K., et al. 2011, ApJ, 737, 73
Fruscione, A., McDowell, J. C., Allen, G. E., et al. 2006, Proc. SPIE, 6270, 62701V
Genzel, R., Eisenhauer, F., & Gillessen, S. 2010, RvMP, 82, 3121
Genzel, R., Schödel, R., Ott, T., et al. 2003, Natur, 425, 934
Ghez, A. M., Hornstein, S. D., Lu, J. R., et al. 2005, ApJ, 635, 1087
Ghez, A. M., Wright, S. A., Matthews, K., et al. 2004, ApJL, 601, L159
Gillessen, S., Eisenhauer, F., Quataert, E., et al. 2006, ApJ, 640, L163
Gillessen, S., Plewa, P. M., Eisenhauer, F., et al. 2017, ApJ, 837, 30
Gravity Collaboration, Abuter, R., Amorim, A., et al. 2018, AAP, 618, L10
Gravity Collaboration, Abuter, R., Amorim, A., et al. 2019, A&A, 625, L10
Gravity Collaboration, Abuter, R., Amorim, A., et al. 2020b, A&A, 638, A2
Gravity Collaboration, Abuter, R., Amorim, A., et al. 2021, A&A, 645, A127
Gravity Collaboration, Bauböck, M., Dexter, J., et al. 2020a, A&A, 635, A143
Haggard, D., Nynka, M., Mon, B., et al. 2019, ApJ, 886, 96
Harrison, F. A., Craig, W. W., Christensen, F. E., et al. 2013, ApJ, 770, 103
Hora, J. L., Witzel, G., Ashby, M. L. N., et al. 2014, ApJ, 793, 120
Hornstein, S. D., Matthews, K., Ghez, A. M., et al. 2007, ApJ, 667, 900
Hunter, J. D. 2007, CSE, 9, 90
Issaoun, S., Johnson, M. D., Blackburn, L., et al. 2019, AAP, 629, A32
Issaoun, S., Johnson, M. D., Blackburn, L., et al. 2021, ApJ, 915, 99
Iwata, Y., Oka, T., Tsuboi, M., Miyoshi, M., & Takekawa, S. 2020, ApJL, 892, L30
Johnson, M. D., Narayan, R., Psaltis, D., et al. 2018, ApJ, 865, 104
Jones, E., Oliphant, T., Peterson, P., et al. 2001, SciPy: Open source scientific tools for Python https://scipy.org/
Kostić, U., Čadež, A., Calvani, M., & Gomboc, A. 2009, AAP, 496, 307
Krabbe, A., Iserlohe, C., Larkin, J. E., et al. 2006, ApJL, 642, L145
Li, Y.-P., Yuan, F., & Wang, Q. D. 2017, MNRAS, 468, 2552
Liu, S., & Melia, F. 2002, ApJL, 566, L77
Liu, S., Petrosian, V., & Melia, F. 2004, ApJL, 611, L101
Maitra, D., Markoff, S., & Falcke, H. 2009, AAP, 508, L13
Markoff, S., Falcke, H., Yuan, F., & Biermann, P. L. 2001, AAP, 379, L13
Marrone, D. P., Baganoff, F. K., Morris, M. R., et al. 2008, ApJ, 682, 373
Marrone, D. P., Moran, J. M., Zhao, J.-H., & Rao, R. 2006, ApJ, 640, 308
Marrone, D. P., Moran, J. M., Zhao, J.-H., & Rao, R. 2007, ApJL, 654, L57
Meyer, L., Do, T., Ghez, A., et al. 2009, ApJL, 694, L87
Meyer, L., Eckart, A., Schödel, R., et al. 2006, AAP, 460, 15
Meyer, L., Schödel, R., Eckart, A., et al. 2007, AAP, 473, 707
Michail, J. M., Wardle, M., Yusef-Zadeh, F., & Kunneriath, D. 2021, ApJ, 923, 54
Mori, K., Gotthelf, E. V., Zhang, S., et al. 2013, ApJL, 770, L23
Mościbrodzka, M., Falcke, H., Shiokawa, H., & Gammie, C. F. 2014, A&A, 570, A7
Mościbrodzka, M., Gammie, C. F., Dolence, J. C., Shiokawa, H., & Leung, P. K. 2009, ApJ, 706, 497
Mossoux, E., Grosso, N., Bushouse, H., et al. 2016, AAP, 589, A116
Murchikova, L., & Witzel, G. 2021, ApJL, 920, L7
Neilsen, J., Nowak, M. A., Gammie, C., et al. 2013, ApJ, 774, 42
Neilsen, J., Markoff, S., Nowak, M. A., et al. 2015, ApJ, 799, 199
Nowak, M. A., Neilsen, J., Markoff, S. B., et al. 2012, ApJ, 759, 95
Ponti, G., De Marco, B., Morris, M. R., et al. 2015, MNRAS, 454, 1525
Ponti, G., George, E., Scaringi, S., et al. 2017, MNRAS, 468, 2447
Quataert, E. 2002, ApJ, 575, 855
Rea, N., Esposito, P., Pons, J. A., et al. 2013, ApJL, 775, L34
Ressler, S. M., Quataert, E., & Stone, J. M. 2020, MNRAS, 492, 3272
Ripperda, B., Liska, M., Chatterjee, K., et al. 2022, ApJL, 924, L32
Rowan, M. E., Sironi, L., & Narayan, R. 2017, ApJ, 850, 29
Scargle, J. D. 1998, ApJ, 504, 405
Scargle, J. D., Norris, J. P., Jackson, B., & Chiang, J. 2013, ApJ, 764, 167
Serabyn, E., Carlstrom, J., Lay, O., et al. 1997, ApJL, 490, L77
Shahzamanian, B., Eckart, A., Valencia-S, M., et al. 2015, AAP, 576, A20
Shcherbakov, R. V., Penna, R. F., & McKinney, J. C. 2012, ApJ, 755, 133
Subroweit, M., García-Marín, M., Eckart, A., et al. 2017, A&A, 601, A80
The Astropy Collaboration, Price-Whelan, A. M., Sipőcz, B. M., et al. 2018, AJ, 156, 123
Trap, G., Goldwurm, A., Dodds-Eden, K., et al. 2011, AAP, 528, A140
Trippe, S., Paumard, T., Ott, T., et al. 2007, MNRAS, 375, 764
van der Laan, H. 1966, Natur, 211, 1131
von Fellenberg, S. D., Gillessen, S., Graciá-Carpio, J., et al. 2018, ApJ, 862, 129
Wang, Q. D., Nowak, M. A., Markoff, S. B., et al. 2013, Sci, 341, 981
Weisskopf, M. C., Tananbaum, H. D., Van Speybroeck, L. P., & O'Dell, S. L. 2000, Proc. SPIE, 4012, 2
Werner, M. W., Roellig, T. L., Low, F. J., et al. 2004, ApJS, 154, 1
Williams, P. K. G., Clavel, M., Newton, E., & Ryzhkov, D. 2017, pwkit: Astronomical utilities in Python, Astrophysics Source Code Library, ascl:1704.001
Witzel, G., Eckart, A., Buchholz, R. M., et al. 2011, AAP, 525, A130
Witzel, G., Eckart, A., Bremer, M., et al. 2012, ApJS, 203, 18
Witzel, G., Martinez, G., Hora, J., et al. 2018, ApJ, 863, 15
Witzel, G., Martinez, G., Willner, S. P., et al. 2021, ApJ, 917, 73
Witzel, G., Morris, M., Ghez, A., et al. 2014, in IAU Symposium, Vol. 303, The Galactic Center: Feeding and Feedback in a Normal Galactic Nucleus, ed. L. O. Sjouwerman, C. C. Lang, & J. Ott (Cambridge: Cambridge Univ. Press), 274
Xu, Y.-D., Narayan, R., Quataert, E., Yuan, F., & Baganoff, F. K. 2006, ApJ, 640, 319
Yoon, D., Chatterjee, K., Markoff, S. B., et al. 2020, MNRAS, 499, 3178
Younsi, Z., & Wu, K. 2015, MNRAS, 454, 3283
Yuan, F., Quataert, E., & Narayan, R. 2003, ApJ, 598, 301
Yusef-Zadeh, F., Bushouse, H., Schödel, R., et al. 2015, ApJ, 809, 10
Yusef-Zadeh, F., Roberts, D., Wardle, M., Heinke, C. O., & Bower, G. C. 2006a, ApJ, 650, 189
Yusef-Zadeh, F., Wardle, M., Cotton, W. D., Heinke, C. O., & Roberts, D. A. 2007, ApJL, 668, L47
Yusef-Zadeh, F., Bushouse, H., Dowell, C. D., et al. 2006b, ApJ, 644, 198
Yusef-Zadeh, F., Bushouse, H., Wardle, M., et al. 2009, ApJ, 706, 348
Yusef-Zadeh, F., Wardle, M., Dodds-Eden, K., et al. 2012, AJ, 144, 1
Zhang, S., Baganoff, F. K., Ponti, G., et al. 2017, ApJ, 843, 96
Zubovas, K., Nayakshin, S., & Markoff, S. 2012, MNRAS, 421, 1315